Dalton Transactions

ROYAL SOCIETY OF CHEMISTRY

PAPER

View Article Online
View Journal | View Issue

Cite this: *Dalton Trans.*, 2026, **55**, 748

Combining coordination and chelation moieties to engineer a new linker for lanthanide coordination chemistry

Ashanthi K. Katuwana Arachchige,[a] Brett Lottes,[a,b] Daniel K. Unruh,[c] Samuel M. Greer,[b] Benjamin W. Stein [b] and Korey P. Carter [*a]

Received 30th October 2025,
Accepted 4th December 2025

DOI: 10.1039/d5dt02620b

rsc.li/dalton

Organic linkers play a crucial role in constructing lanthanide (Ln) coordination polymers (CPs), influencing structural topologies and physicochemical properties. Herein, we introduce 6-oxo-1,6-dihydro-2,5-pyridinedicarboxylic acid (2,5-H_3PODC) as a new ligand for constructing lanthanide coordination polymers that integrates the structural features of terephthalic acid with the chelation capabilities of pyridinone-based functional groups. Six lanthanide-based coordination polymers were synthesized with 2,5-H_3PODC, forming two types of CPs – **type 1**: [Ln(HPODC)$(Ox)_{0.5}(H_2O)_2$] (where (Ox) = oxalic acid and Ln = Pr^{3+} (**1**), Nd^{3+} (**2**)) and **type 2**: [Ln(H_2PODC)(HPODC)(H_2O)] (Ln = Eu^{3+} (**3**), Gd^{3+} (**4**), Dy^{3+} (**5**), Er^{3+} (**6**)). All compounds were structurally characterized by single-crystal and powder X-ray diffraction, and both compound types are 2D ladder-like networks with **cem** topologies where the trivalent metal centers are bridged *via* $HPODC^{2-}$ and Ox^{2-} ligands in **type 1** structures and H_2PODC^- and $HPODC^{2-}$ linkers in **type 2** structures. Thermogravimetric analysis (TGA) demonstrated that the metal–organic networks of **type 1** and **type 2** compounds exhibit distinct decomposition patterns, and the photoluminescent properties of **3** were also examined, revealing efficient ligand based sensitization and characteristic emission bands for Eu(III).

Introduction

The synthesis and characterization of lanthanide (Ln) based coordination polymers is an area of sustained research interest owing to their diverse structural configurations and promising applicability as functional materials in sensors,[1–6] gas capture and separations,[7–10] and catalysis.[11–15] Coordination polymers (CPs) are a well-known class of organic–inorganic hybrid materials built from metal cations or clusters connected by polytopic organic linkers. Generally, the coordination environment provided by the donor atoms in the functional groups of the organic linker needs to match the geometric preferences of the metal cation to facilitate the construction of one, two-, or three-dimensional CPs. This is a distinct challenge and opportunity when lanthanides are included in hybrid materials as the larger coordination spheres and flexible coordination geometries of Ln(III) cations facilitate access to unique structural topologies;[16,17] however, ligands often need to be tailored for metal-ion binding that also allows for the realization of the distinctive electronic, magnetic, and optical characteristics of the 4f elements.[18–22] Lanthanide cations are known for their oxophilicity, and multitopic carboxylic acid ligands have been the most common linker choice for the synthesis of Ln^{3+} CPs.[23–31] Early studies predominantly featured benzene-based polycarboxylic ligands, such as terephthalic acid, which are synthetically accessible and commercially available.[32–37] More recently, heteroaromatic carboxylic ligands featuring pyridine, furan, and thiophene moieties have also proven to be useful for constructing lanthanide CPs with a range of notable structures, topologies, assembly mechanisms, and properties such as enhanced photophysical characteristics.[23,38–48]

Within the field of hybrid materials, there has been recent interest in developing new routes for incorporating different moieties into ligand structures *via* the process of linker engineering, which involves tailoring ligand structures to facilitate synthesis of coordination polymers (CPs) and metal–organic frameworks with desired properties.[49–52] Linker engineering can be achieved *via* multiple pathways, and one effective approach is to introduce specific moieties ahead of CP or MOF synthesis, wherein the desired functional groups are incorporated into the organic linker structure prior to metal complexation.[49,50] Carboxylate linkers offer nearly limitless

[a]*Department of Chemistry, University of Iowa, Iowa City, IA 52242, USA. E-mail: korey-carter@uiowa.edu*
[b]*Los Alamos National Laboratory, P.O. Box 1663, Los Alamos, NM 87545, USA*
[c]*Office of the Vice President for Research, University of Iowa, Iowa City, IA 52242, USA*

functionalization potential as illustrated by tailored examples bearing pyridyl,[5,53,54] amine,[55,56] amide,[57] azide,[58] hydroxyl,[59,60] alkyl,[61] or halogen[62] moieties, all of which have been used in the construction of novel f-block CPs. Engineering of linkers beyond carboxylate based systems are considerably less common, and in particular, pyridinone-functionalized linkers are notably absent from the transition metal and lanthanide hybrid material literature. This research gap, coupled with our interest in the coordinative abilities of siderophore molecules in nature that contain catechol, hydroxamate, and other similar functional groups, prompted us to investigate the influence of pyridinone-based ligands on lanthanide coordination chemistry.[63,64]

To allow for a more direct comparison with established results in the literature, we synthesized a ligand, 6-oxo-1,6-dihydro-2,5-pyridinedicarboxylic acid (2,5-H_3PODC), featuring a pyridinone moiety added to the well-known terephthalic acid scaffold. While the ligand has been previously described,[65] it has not been used in any inorganic coordination compounds and there was a need to update the ligand synthesis process to enable broader use. Linkers of this type can be partially or fully deprotonated to generate H_2PODC^-, $HPODC^{2-}$, and $PODC3^-$ ligands, depending on the pH of the medium employed, and the resulting structures and topologies can be engineered *via* judicious control of reaction pH values. Moreover, the introduction of N–H and carbonyl functionalities in 2,5-H_3PODC provide additional routes for non-covalent assembly through well-known motifs such as hydrogen bonding, and 2,5-H_3PODC possesses hydrogen bond donor and acceptor sites within the same linker, thereby increasing the pathways for accessing hybrid materials with novel structures and topologies.

Herein we describe the modified synthesis of 2,5-H_3PODC and the first successful incorporation of a PODC ligand in an inorganic coordination compound. Six coordination polymers containing a range of Ln^{3+} metal ions (Pr^{3+}, Nd^{3+}, Eu^{3+}, Gd^{3+}, Dy^{3+}, Er^{3+}) were obtained from solvothermal reactions, and the resulting structures adopt one of two main structure types: **type 1** $[Ln(HPODC)(Ox)_{0.5}(H_2O)_2]_n$ (where (Ox) = oxalic acid and Ln = Pr^{3+} (**1**), Nd^{3+} (**2**)) and **type 2** $[Ln(H_2PODC)(HPODC)(H_2O)]_n$ (Ln = Eu^{3+} (**3**), Gd^{3+} (**4**), Dy^{3+} (**5**), Er^{3+} (**6**)). All compounds were structurally characterized *via* single-crystal X-ray diffraction (SCXRD) and powder X-ray diffraction (PXRD), and crystallographic data revealed that **1–6** crystallized in the $P\bar{1}$ space group and formed 2D layered structures with **cem** topologies. The thermal properties of **1–6** were investigated, revealing two distinct decomposition patterns for **type 1** and **type 2** compounds. Additionally, photoluminescence properties for compound **3** were investigated, and characteristic emission bands for Eu(III) were observed upon 2,5-H_3PODC sensitization. Overall, our findings demonstrate that 2,5-H_3PODC is an effective ligand for the fabrication of Ln CPs, integrating the coordination features of carboxylic acid-based ligands with the chelation ability of pyridinone functional groups, and this study highlights the potential of linker engineering in the design of functional Ln CPs.

Experimental

Materials and methods

All chemicals were commercially available and were used as received. Chemicals used in the 2,5-H_3PODC ligand synthesis process include 2-chloro-6-methyl nicotinic acid (Ambeed Inc., 99.9%), potassium hydroxide (Sigma Aldrich, ≥85%), potassium permanganate (Sigma Aldrich, ≥99%), and hydrochloric acid 37% (w/w) (Sigma Aldrich). Ligand complexation with lanthanide cations involved either Ln(III) nitrate (Ln = Pr^{3+}, Nd^{3+}, Eu^{3+}) or chloride (Gd^{3+}, Dy^{3+}, Er^{3+}) salts, which were purchased from either Strem Chemicals Inc. or Beantown Chemical and were at least 99.9% pure. Oxalic acid (H_2Ox) was laboratory grade and purchased from Ward's Science, while ethanol (EtOH) (Decon Labs Inc., 100%) was used without distillation, and water was obtained from a Milli-Q IQ 7000 purification system.

^1H and ^{13}C NMR spectra were recorded on a Bruker Avance NEO 400 spectrometer operating at 400 MHz using deuterated solvents. The data for ^1H NMR spectra are presented as follows: chemical shift (δ ppm) relative to a Me_4Si standard, multiplicity denoted by abbreviations such as br (broad), s (singlet), d (doublet), or t (triplet), coupling constant (Hz), and integration. High resolution mass spectra (HRMS) were recorded using a Thermo Q-Exactive mass spectrometer with an electrospray ionization source (ESI) operating in negative ionization mode using Optima (Fisher Chemical) grade solvents.

Powder X-ray diffraction samples were collected on a Bruker D8 Advanced diffractometer with samples loaded on KS Analytics zero background holders. The instrument is equipped with Göbel Mirrors and the data were collected using a monochromatic Cu K_α X-ray source, λ = 1.5406 Å. Data collections were performed over the range 5°–60° two-theta at a scanning speed of 0.5 seconds per step. Data were baseline corrected using the PreDICT software[66] package and diffractograms were prepared in Origin 2024.[67]

After confirming the bulk purity of the materials, infrared spectra for **1–6** were collected in both the mid-IR (MIR) (4000–500 cm^{-1}) and far-IR (FIR) (400–100 cm^{-1}) spectral regions on a Bruker VERTEX 70 V spectrometer equipped with a platinum attenuated total reflectance microscope objective and the OPUS 8.5 software package. The resolution for MIR and FIR measurements were 0.4 cm^{-1} and 1 cm^{-1}, respectively, and spectra were prepared for publication using Origin 2024.

The elemental composition of compounds **1–6** were further analyzed *via* energy dispersive spectroscopy (EDS) with a JEOL JSM-1T700HR field emission scanning electron microscope (FE-SEM). Samples from bulk powders of **1–6** were placed on aluminum stubs with double-sided carbon tape and were not coated prior to the analysis. The operating voltage was 15 kV and a backscattered electron detector (BED-C) in low-vacuum (40 Pa) mode was used for data collection at a constant working distance of 10 mm.

Thermogravimetric analysis of compounds **1–6** was performed on a differential thermogravimetric analyzer (SDT)

Q600 instrument in an air atmosphere with a flow rate of 50 mL min^{-1} and a heating rate of 10 °C min^{-1}. Prior to analysis, powdered samples of compounds **1–6** were purified with 2 mL of Milli-Q water (repeated five times) to remove minor organic and inorganic impurities. The TGA spectra were processed and prepared for publication using Origin 2024.

Elemental analysis (C, H, and N) measurements for purified compounds **1–6** were performed on an Exeter Analytical CE440 CHN analyzer. Crystalline powders of all compounds (2–3 mg) were weighed into tin sample holders and sealed securely with a capsule press. The samples were then transferred into the instrument and combusted in an oxygen-rich atmosphere.

Photoluminescence data for compound **3** was collected at room temperature on an Edinburgh Instruments FLS1000 spectrometer using the Fluoracle software package. Emission spectra were collected using a 279 nm excitation wavelength for the luminescence standard, $Na_3Eu(dipic)_3$ (dipic = dipicolinate), and a 368 nm excitation wavelength for **3**. Solid-state measurements were conducted on crystalline material from the bulk product of **3** using a microscope attachment with 20× magnification and a dichroic mirror over the 400–800 nm spectral window using a 0.1 nm step size. Solution state data were collected to determine the relative quantum yield for **3** and this data collection was performed using a 1 cm quartz cuvette and 75 μM solution concentrations, and data were collected over a spectral window of 250–700 nm. Solid state luminescence data were collected with excitation and emission bandwidths of 2 nm, while solution state data were obtained using excitation and emission slit widths of 1 nm. The quantum yield for complex **3** was measured using the conventional optical method, where the quantum yield is determined relative to a fluorescent standard, $Na_3Eu(dipic)_3$, with a known quantum yield. A detailed procedure for this process is provided in the SI.

Synthesis of 6-oxo-1,6-dihydro-2,5-pyridinedicarboxylic acid (2,5-H_3PODC)

2,5-H_3PODC synthesis was achieved *via* a two-step procedure (Scheme 1). We adapted a literature procedure to obtain **1a** in the first step,[68] and pure **1a** (1.509 g, 7.48 mmol) was then suspended in 10 mL of water with stirring and 11 mL of 37% HCl was added dropwise. Subsequently, the reaction mixture was stirred for twelve hours at 110 °C and a white precipitate was observed. The precipitate was recovered by gravity filtration, washed with cold water, and air dried for one day to obtain a solid white product. Overall Yield: 79%. ^{1}H-NMR (400 MHz, DMSO-d_6); δ = 14.00 (br, s, 2H), 8.45(d, J = 7.6 Hz, 1H), 7.23 (d, J = 7.2 Hz, 1H). ^{13}C-NMR (400 MHz, D_2O–NaOH); δ = 177.6, 174.3, 167.8, 152.0, 137.3, 126.1, 109.4. HRMS-ESI (m/z, [M − H]$^-$) calculated for $C_7H_5NO_5$: 182.0095, found: 182.0095 (Fig. S1–S3, SI). Additional characterization of 2,5-H_3PODC, including PXRD and FIR/MIR spectra, is provided in the SI (Fig. S4–S6, SI).

Synthesis of compounds 1–6

$[Pr(HPODC)(Ox)_{0.5}(H_2O)_2]_n$ (1). A mixture of $Pr(NO_3)_3{\cdot}6H_2O$ (0.0200 g, 0.046 mmol), 2,5-H_3PODC (0.0208 g, 0.114 mmol), H_2O (5 mL), and EtOH (1 mL) were placed in a 23 mL Teflon lined Parr autoclave, and the reaction vessel was heated at 120 °C for three days under autogenous pressure. After slow cooling overnight, the autoclave was opened and a pale green solution with a pale yellow precipitate was observed. The reaction solution was then transferred into a 20 mL glass scintillation vial and allowed to slowly evaporate for fifteen days, which yielded pale green block shaped single crystals of **1** suitable for single crystal X-ray diffraction (SCXRD) analysis. Yield: 9.50 mg, 52% based on Pr. Anal. calcd (%) for $C_8H_7NO_9Pr$: C, 23.9; H, 1.76; N, 3.48. Found (%): C, 23.59; H, 1.65; N, 3.35.

$[Nd(HPODC)(Ox)_{0.5}(H_2O)_2]_n$ (2). Compound **2** was synthesized following the procedure described for **1** except Nd $(NO_3)_3{\cdot}6H_2O$ (0.0201 g, 0.046 mmol) was used instead of Pr $(NO_3)_3{\cdot}6H_2O$ and the amount of 2,5-H_3PODC (0.0201 g, 0.109 mmol) was slightly adjusted. Colorless block shaped crystals of **2** suitable for SCXRD analysis were obtained after slow evaporation of the solvothermal reaction solution for twelve days. Yield: 9.48 mg, 51% based on Nd. Anal. calcd (%) for $C_8H_7NO_9Nd$: C, 23.7; H, 1.74; N, 3.46. Found (%): C, 23.75; H, 1.64; N, 3.43.

$[Eu(H_2PODC)(HPODC)(H_2O)]_n$ (3). Compound **3** was synthesized following the procedure described for **1** except Eu $(NO_3)_3{\cdot}6H_2O$ (0.0200 g, 0.045 mmol) was used instead of Pr $(NO_3)_3{\cdot}6H_2O$ and the amount of 2,5-H_3PODC (0.0198 g, 0.108 mmol) was decreased. Colorless block shaped crystals of **3** suitable for SCXRD analysis were obtained after slow evaporation of the solvothermal reaction solution for twelve days. Yield: 13.20 mg, 55% based on Eu. Anal. calcd (%) for $C_{14}H_9EuN_2O_{11}$: C, 31.54; H, 1.70; N, 5.25. Found (%): C, 31.16; H, 1.68; N, 5.1.

$[Gd(H_2PODC)(HPODC)(H_2O)]_n$ (4). Compound **4** was synthesized following the procedure described for **1** except $GdCl_3{\cdot}6H_2O$ (0.0252 g, 0.067 mmol) was used instead of Pr $(NO_3)_3{\cdot}6H_2O$ and the amount of 2,5-H_3PODC (0.0251 g,

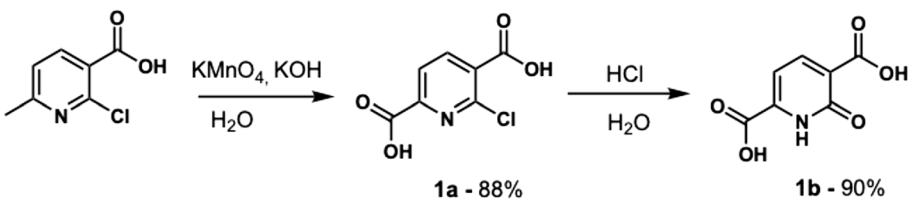

Scheme 1 Two step synthetic process used herein to prepare 2,5-H_3PODC.

0.137 mmol) was increased. Colorless block shaped crystals of **4** suitable for SCXRD analysis were obtained after slow evaporation of the solvothermal reaction solution for eight days. Yield: 29.93 mg, 83% based on Gd. Anal. calcd (%) for $C_{14}H_9GdN_2O_{11}$: C, 31.23; H, 1.68; N, 5.2. Found (%): C, 30.93; H, 1.66; N, 5.0.

$[Dy(H_2PODC)(HPODC)(H_2O)]_n$ (5). A mixture of $DyCl_3{\cdot}6H_2O$ (0.0253 g, 0.067 mmol), 2,5-H_3PODC (0.0285 g, 0.155 mmol), H_2O (5 mL), and EtOH (1 mL) were placed in a 23 mL Teflon lined Parr autoclave, and the reaction vessel was heated at 120 °C for three days under autogenous pressure. After slow cooling overnight, the autoclave was opened and yellow block shaped crystals of **5** were observed that were suitable for SCXRD analysis. Yield: 22.90 mg, 63% based on Dy. Anal. calcd (%) for $C_{14}H_9DyN_2O_{11}$: C, 30.93; H, 1.67; N, 5.15. Found (%): C, 30.53; H, 1.66; N, 4.97.

$[Er(H_2PODC)(HPODC)(H_2O)]_n$ (6). Compound **6** was synthesized following the procedure described for **5** with a mixture of $ErCl_3{\cdot}6H_2O$ (0.0258 g, 0.067 mmol), 2,5-H_3PODC (0.0271 g, 0.148 mmol), H_2O (5 mL), and EtOH (1 mL) added into a 23 mL Teflon lined Parr autoclave. The reaction was heated at 120 °C for three days under autogenous pressure, and after slow cooling overnight, the autoclave was opened and pink block shaped crystals of **6** were observed that were suitable for SCXRD analysis. Yield: 20.55 mg, 56% based on Er. Anal. calcd (%) for $C_{14}H_9ErN_2O_{11}$: C, 30.66; H, 1.65; N, 5.11. Found (%): C, 30.27; H, 1.65; N, 4.92.

Bulk purification of compounds 1–6

After isolation, the crystalline solids were washed with deionized water (2 mL × 5) to remove water soluble impurities. SEM-EDS analysis of bulk samples indicated trace amounts of inorganic impurities (Fig. S21, SI); therefore, all compounds were purified through repeated water washes until the impurities were removed and no longer detected in SEM-EDS analysis (Fig. S22–S27, SI). The resulting purified solids were used for TGA and elemental analysis data collection.

Single crystal X-ray diffraction studies

X-ray diffraction data collection for compounds **1–6** were obtained on a Bruker D8 Venture Duo diffractometer equipped with a IμS 3.0 microfocus source operated at 75 W (50 kV, 1.5 mA) to generate Mo Kα radiation (λ = 0.71073 Å) and a PHOTON III detector. Crystals suitable for SCXRD were selected for each compound using a Zeiss Stemi 305 microscope and transferred from sample vials to glass slides in NVH immersion oil. For **1–6**, single crystals and a small amount of oil were collected on MiTeGen 100-micron MicroLoops and transferred to the instrument where they were placed under a cold nitrogen stream (Oxford 800 series) maintained at 100(2) K throughout the duration of the experiments. Optimal alignment of crystals for each compound was achieved with the assistance of a video camera to ensure no translations occurred while crystals were rotated through all positions. Absorption corrections were applied to data collected for **1–6** using the SADABS multi-scan method within APEX 5.[69] SHELXT[70] was used for the initial structure solution by direct methods and SHELXL[71] was used for refinement of structures contained within the Olex2 1.3 software suite.[72] Anisotropic thermal parameters were assigned to all lanthanide, carbon, oxygen, and nitrogen atoms. Hydrogen atoms bound to carbon and nitrogen atoms were located in difference Fourier maps and were geometrically constrained using the appropriate AFIX commands. In the structure of compound **4**, based on the C14–O10 bond distance and overall charge balance of the structure, H9 was located initially *via* difference Fourier map and refined using DFIX and DANG restraints. Similar procedures were followed for all **type 2** compounds to locate hydrogen atoms on the carboxylic groups. Crystallographic information and selected bond distances and angles for compounds **1–6** can be found in Tables S1–S3 (SI). CIF files for **1–6** have been deposited at the Cambridge Crystallographic Database Center (CCDC) and may be obtained from https://www.ccdc.cam.ac.uk by citing reference numbers 2428551–2428556. CrystalMaker[73] was used to generate all figures for compounds **1–6**, while Mercury[74] was used specifically for the asymmetric unit representations. Topological analysis of compounds **1** and **4** was performed using the topology identification software, ToposPro 5.5.2.2.[75] The standard simplification method was applied wherein structural groups were reduced to their respective centers of mass. In both compounds, metal atoms were designated as the central nodes, maintaining their original positions, while organic ligands and coordinated water molecules were simplified by representing them at their respective centers of mass.

Results and discussion

Structural descriptions

$[Ln(HPODC)(Ox)_{0.5}(H_2O)_2]_n$ where Ln = Pr^{3+}, Nd^{3+} – compound type 1. Solvothermal reactions of Pr^{3+} and Nd^{3+} with 2,5-H_3PODC followed by slow evaporation of reaction solutions yielded compounds **1** and **2**, which are isomorphous and crystallize in the $P\bar{1}$ space group. To highlight the key features of **type 1** structures, we will use compound **1** as a representative example and describe the specifics of this structure in detail. The asymmetric unit of compound **1** contains one Pr^{3+} ion, one $HPODC^{2-}$ unit with fully deprotonated carboxylate groups, one half of an oxalate ligand, and two coordinated water molecules (Fig. 1a). The Pr^{3+} center is crystallographically unique and has a coordination number of nine, and the molecular geometry of the metal center can best be described as capped square antiprismatic (Fig. 1b).

Four oxygen atoms from carboxylate moieties of PODC ligands [O1, O8, O8 ($-x$, $1-y$, $2-z$), O9], one oxygen atom from a carbonyl group (O7) of a PODC ligand, two oxygen atoms from one oxalate group (O4, O5), and two oxygen atoms from coordinated water molecules (O2, O3) comprise the Pr^{3+} first coordination sphere. The Pr–O (COO–), Pr–O (carbonyl), and Pr–O (H_2O) bond lengths are in the range 2.357(2) Å–2.702 (2) Å, and the bond lengths in **1** are comparable to those in

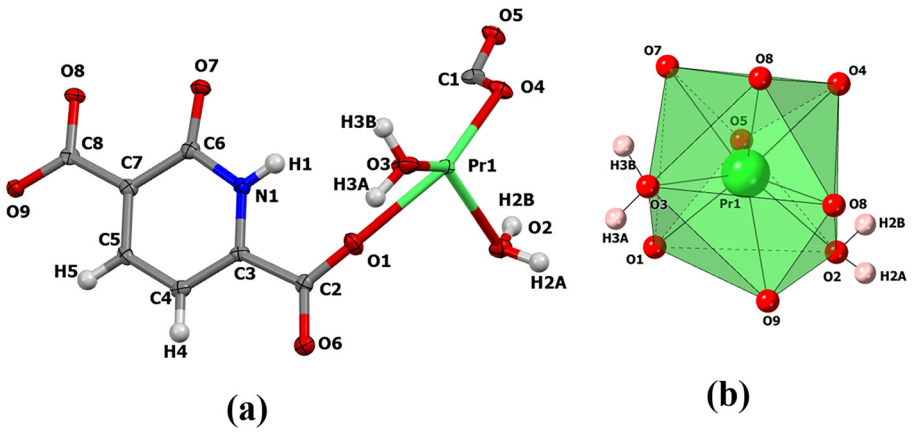

Fig. 1 (a) Ellipsoid representation of the asymmetric unit of compound **1** shown at 50% probability level and (b) polyhedral representation of coordination geometry around the Pr^{3+} center.

Pr^{3+}-2,5-pyridinedicarboxylate compounds described in the literature.[76] The two adjacent Pr^{3+} metal centers in **1** are bridged in a *syn–syn* fashion *via* carboxylate O atoms (O8) from two adjacent $HPODC^{2-}$ units at a distance of 4.215 Å (Fig. 2). This results in the formation of dinuclear secondary building units (SBUs) in **1**, and the structure of **1** also features a bound oxalate ligand, which plays a crucial role in the construction of the two-dimensional sheets that ultimately form. Oxalate ligands were generated *in situ*, indicating the partial decomposition of 2,5-H_3PODC under experimental solvothermal conditions, and a proposed ring-opening/hydrolysis-oxidation mechanism for the *in situ* generation of oxalate is described in the SI (Scheme S1).[77]

Within compound **1**, the PODC ligand was found in only one protonation state, $HPODC^{2-}$, and it adopts only one coordination mode, μ_3-η^1:η^2:η^2, wherein it acts as a μ_3-bridge that connects three Pr^{3+} centers (Fig. S9, SI). Here, both carboxylic groups are deprotonated, with the carboxylate group at the 2-position binding in a monodentate fashion to one Pr^{3+} center, while the second carboxylate group adopts a chelating–bridging coordination motif to link another Pr^{3+} metal center. The third Ln^{3+} center is bound in a bidentate fashion to two adjacent O donor atoms from carboxylic acid and carbonyl groups, adopting a salicylate chelation mode. The second linker in **type 1** structures, Ox^{2-} units, bind to Pr^{3+} centers in a bidentate bridging fashion *via* a μ_2-η^2:η^2 coordination mode (Fig. S9, SI). The 2D network in **1** is built from bridged Pr^{3+} metal centers that are connected through oxalate ligands to form 1D layers that propagate along the *c* direction (Fig. 3a). The 1D layers in **1** are further linked diagonally by $HPDOC^{2-}$ ligands, extending along the *a* direction to yield a 2D sheet structure (Fig. 3b). Topologically, each Pr^{3+} center serves as a five-connected node, whereas the $HPODC^{2-}$ and Ox^{2-} ligands act as two-connected nodes, and the coordinated water molecules function as one-connected nodes (see Fig. S11, SI). Based on this simplification, the overall structure can be described as a five-connected uninodal network with a **cem** topology. According to data from the CCDC and TopoCryst databases,[78,79] this topology is unusual for lanthanide-based CPs with only one example previously described.[80]

The 2D network in **1** is further reinforced by hydrogen bonding interactions between PODC ligand functional groups

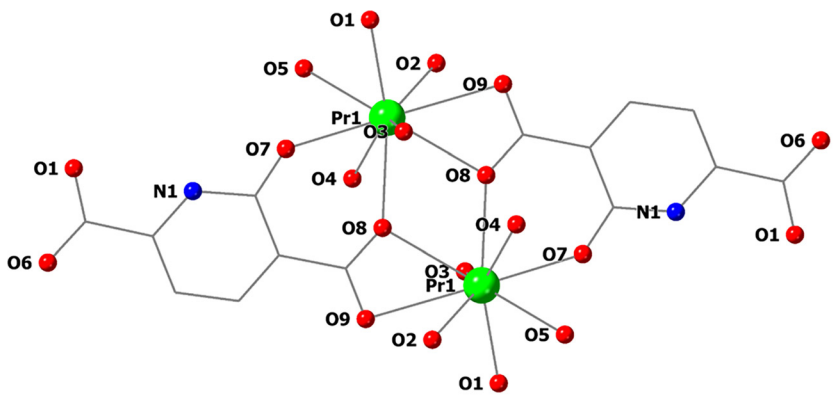

Fig. 2 Ball and stick representation of **1** highlighting the bridging carboxylate oxygen atoms connecting Pr^{3+} metal centers to form a dinuclear secondary building unit.

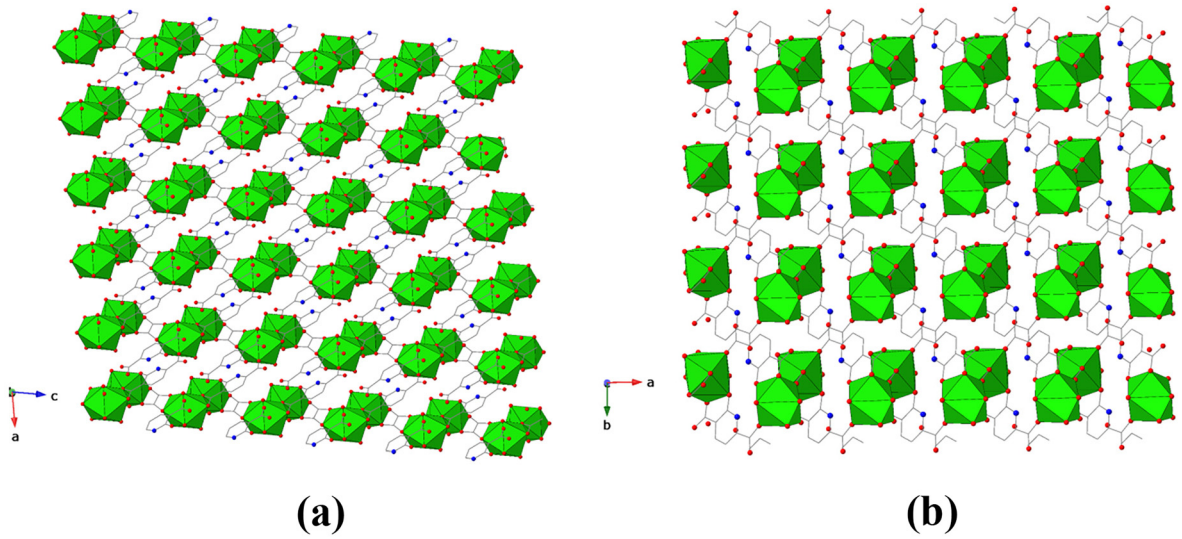

Fig. 3 (a) Polyhedral representation of **1** illustrating the connectivity of Pr^{3+} centers in the *ac* plane and (b) *ab* plane. Green polyhedra represent Pr^{3+}, whereas red and blue spheres represent oxygen and nitrogen atoms, respectively. H atoms have been omitted for clarity.

and coordinated water molecules. Three hydrogen bonding interactions were observed in compound **1**, and non-covalent interaction details for this structure type are compiled and tabulated in Table S4 (SI). The two strongest H-bonding interactions, based on crystallographic metrics, in **type 1** structures are intermolecular O–H···O interactions that involve protons from coordinated water molecules, O3–H3A and O2–H2A, serving as hydrogen bond donors, while O6 from a PODC carboxylate group acts as a hydrogen bond acceptor for both interactions (Fig. S13a, SI). Collectively, these two hydrogen bonding interactions enhance the connectivity of **type 1** structures within the layers in the *ac*-plane. An additional O–H···O interaction occurs between O3–H3B and a bound water molecule (O3) on the neighboring Pr^{3+} SBU that further reinforces network assembly along the *a*-axis (Fig. S13b, SI).

$[Ln(H_2PODC)(HPODC)(H_2O)]_n$ where Ln = Eu^{3+}, Gd^{3+}, Dy^{3+}, Er^{3+} – compound type 2. Single crystal X-ray crystallographic data revealed that compounds **3–6** are isomorphous and crystallize in the $P\bar{1}$ space group. To highlight the key features of **type 2** structures, we will use compound **4** as a representative example and describe the specifics of this structure in detail. The asymmetric unit of compound **4** consists of one Gd^{3+} cation, two PODC ligand units that differ in their extent of protonation, and a bound water molecule. More specifically, we observe one doubly protonated H_2PODC^- moiety as well as a singly protonated $HPODC^{2-}$ ligand that are both bound to the Gd^{3+} metal center (Fig. 4a). The first coordination sphere, shown in Fig. 4b, for Gd^{3+} reveals that the metal-ion has a coordination number of eight and adopts distorted square antiprismatic molecular geometry, wherein five oxygen atoms from PODC carboxylate groups of five ligand units (O1, O2, O4, O8, O11), two oxygen atoms from carbonyl groups (O6, O9) of different neighboring PODC ligands, and one oxygen atom from a coordinated water molecule (O3) all bind to the metal center. The reduction in the coordination number of the metal center from nine to eight in **type 2** structures is a result of the

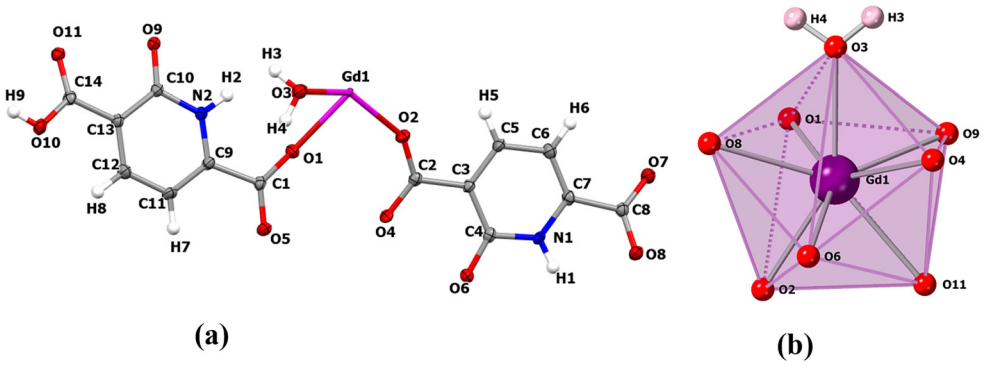

Fig. 4 (a) Ellipsoid representation of the asymmetric unit for compound **4** shown at 50% probability level and (b) polyhedral representation of coordination geometry around the Gd^{3+} center.

well-known lanthanide contraction, and the Gd–O (COO–), Gd–O (carbonyl), Gd–O (H_2O) bond lengths in **4** range from 2.296(2) Å–2.382(2) Å, with the longest bond lengths observed for Gd–carbonyl group coordination. The lengthening of the Gd–carbonyl (Gd–O6, 2.380(2) Å and Gd–O9 2.382(2) Å) bonds in **4** may be due to carbonyl oxygen atom participation in hydrogen bonding interactions with the protonated pyridine groups on neighboring PODC ligands since H-bonding interactions can affect the electron density distribution across the PODC ring, leading to slight geometric changes that also ultimately impact Gd–O (carbonyl) bond lengths.

Compounds that adopt **type 2** structures feature PODC ligands in two protonation states, H_2PODC^- and $HPODC^{2-}$, with differences manifesting in distinct metal-ion coordination modes. The $HPODC^{2-}$ moiety adopts a different binding configuration compared to what was observed in **type 1** structures, wherein three Ln^{3+} metal centers are connected in a μ_3-η^2:η^1:η^1 fashion and both oxygen atoms in the carboxylate group at the 5-position participate in bridging bidentate coordination to two Gd^{3+} metal centers. In contrast, the H_2PODC^- unit features a protonated carboxylate group at the 5-position and coordinates to two Gd^{3+} metal cations in a μ_2-η^2:η^1 fashion (Fig. S10, SI). This moiety exhibits the same salicylate coordination mode and monodentate coordination by the 2-position carboxylate group that was observed in the $HPODC^{2-}$ moiety in **type 1** structures, and the combination of PODC coordination modes provide extensive opportunities for mononuclear Gd^{3+} metal centers to assemble, thereby laying the foundation for the formation of a 2D extended network.

Analysis of the extended structure of **4** reveals that monomeric Gd^{3+} centers are linked by two H_2PODC^- units to produce a 1D layer that extends along the *c*-axis (Fig. 5a). These 1D chains are further connected along the *a*-axis by Gd–O bonds from the carboxylate group of $HPODC^{2-}$ units to create a 2D sheet (Fig. 5b). Each of the 2D sheets that extend along the *c*-direction are further linked through hydrogen bonds that involve the proton (H9) in the carboxylic acid group of the H_2PODC^- unit and the oxygen (O7) in the neighboring $HPODC^{2-}$ unit to form a 3D supramolecular network (Fig. 5c). Topological analysis revealed that compound **4** features a five-connected uninodal net with a **cem** topology, similar to compound **1**. In this structure, Gd^{3+} centers act as five-connected nodes, while H_2PODC^- ligands function as two-connected nodes, $HPODC^{2-}$ linkers function as three-connected nodes, and bound H_2O molecules act as one-connected nodes (see Fig. S12, SI). Despite the differences between **type 1** and **2** structures, the

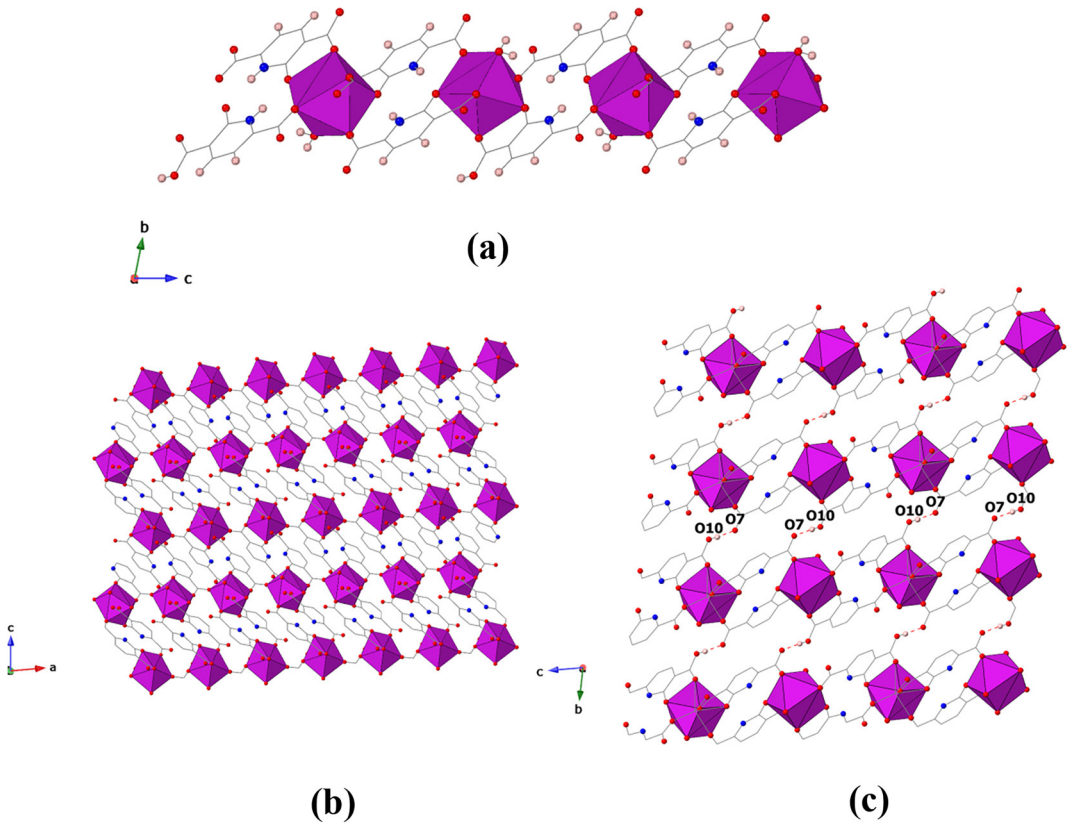

Fig. 5 (a) Polyhedral representation of **4** showing 1D chains that are linked along the *c*-axis and (b) 2D coordination network of **4** in the *ac* plane. (c) Polyhedral representation of **4** showing hydrogen bonding interactions that further link the 2D sheets of **4** in the *bc* plane (atoms involved in O10–H9···O7 hydrogen bonding interactions are labelled in only one layer for clarity) to form a hydrogen bonding 3D framework. Purple polyhedra represent Gd^{3+}, whereas red, blue, and pink spheres represent oxygen, nitrogen, and hydrogen atoms, respectively. H atoms outside of H9 have been omitted for clarity in parts b and c of the figure.

metal centers in **1** and **4** are 5-connected nodes with a similar number of three-, four-, and five membered faces surrounding each metal center (point symbol – $3^3{\cdot}4^4{\cdot}5^3$), which is why **type 1** and **2** structures feature the same overall topology.

The assembly of compound **4** is further supplemented by three additional hydrogen bonding interactions. The first one is an intramolecular hydrogen bonding interaction where the hydrogen atoms on bound water molecules (O3) act as hydrogen bond donors and neighboring O5 atom of a PODC carboxylate group acts as a H-bond acceptor (O3–H3···O5–2.657(4) Å). In addition, two N–H···O hydrogen bonds were observed, and these involve donor protons H1 (from the N1 site of $HPODC^{2-}$) and H2 (from the N2 site of H_2PODC^{2-}), interacting with acceptor oxygen atoms O9 and O6 from adjacent carbonyl groups (N2–H2···O9–2.855(4) Å, N1–H1···O6–2.891(4) Å). From a structural perspective, the N–H···O interactions enhance the connectivity between the ligand units within the same layer along the *b*-axis (Fig. S14, SI), and all the hydrogen bonding interactions observed collectively enhance the connectivity of the 3D supramolecular networks in **type 2** structures.

Structural discussion

The extended networks in both **type 1** and **type 2** structures can best be described as two-dimensional sheets with ladder-like networks, having pore sizes of 5.822 Å × 6.917 Å (**type 1**, compound **2**) and 6.177 Å × 9.053 Å (**type 2**, compound **4**), respectively (Fig. 6). These structures feature non-catenated interlayer spaces, making them particularly promising for applications such as gas sorption, sensing, and water purification when constructed with suitable metals. Several key features could contribute to their performance in these areas including large voids that are accessible to guest or substrate molecules and N–H groups and carboxylate oxygen atoms of 2,5-H_3PODC that remain uncoordinated to metal centers and oriented toward the voids, which could serve as Lewis basic centers for recognizing Lewis acidic molecules that are relevant in environmental remediation and catalysis.

Analysis of **type 1** and **type 2** structures shows that 2,5-H_3PODC ligands impact the primary coordination sphere and the secondary hydrogen bonding network within **1–6**, directing assembly toward distinct topologies compared to well-documented lanthanide CPs constructed using 2,5-pyridinedicarboxylic acid (2,5-PDC). With 2,5-PDC linkers, lanthanide coordination occurs primarily through the carboxylate oxygens and the nitrogen atom on the heterocycle.[81–85] For 2,5-H_3PODC, we note binding *via* carboxylic acid oxygen atoms as well as additional coordination *via* the carbonyl oxygen atom from the pyridinone moiety that facilitates salicylate-like binding in both its protonation states, H_2PODC^- and $HPODC^{2-}$. Notably, despite the precedent for nitrogen coordi-

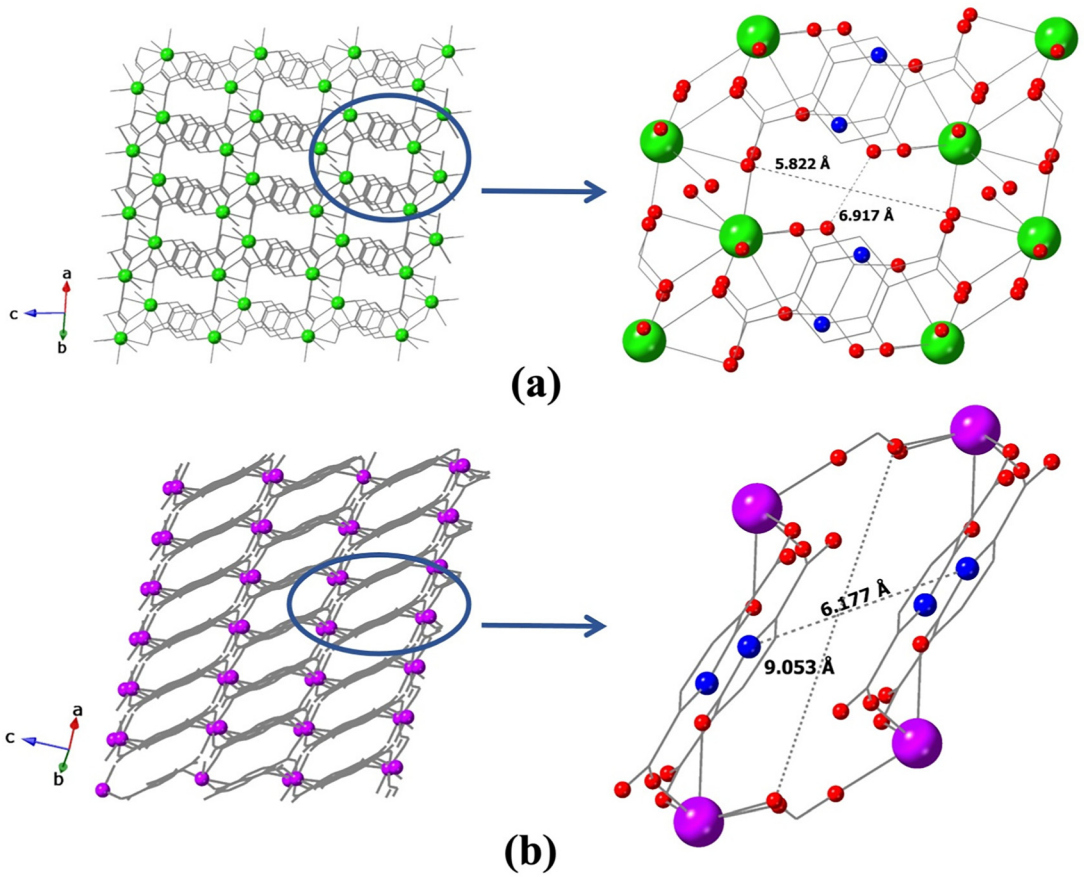

Fig. 6 2D ladder-like network and the structure of the voids in (a) **type 1** and (b) **type 2** structures.

nation in 2,5-PDC systems, no such coordination was observed in **1–6**.

Beyond definitive differences in ligand coordination modes, 2,5-H_3PODC also expands the supramolecular landscape compared to 2,5-PDC in lanthanide hybrid materials. Supramolecular networks, particularly hydrogen-bonded organic frameworks (HOFs), have been gaining significant attention in the field of functional materials. HOFs are porous structures assembled through directional intra- and intermolecular hydrogen bonding interactions that are typically driven by organic ligand moieties. These networks are distinguished by their weak and reversible bonding, which imparts unique properties such as flexibility, easy regeneration, and solution processability. Consequently, HOFs have demonstrated promise in various applications, including gas separation, molecular storage, catalysis, and drug delivery.[86,87] The primary strategy for synthesizing HOFs involves the incorporation of functional groups that can act as hydrogen bond donors and acceptors. In this context, 2,5-H_3PODC can be presented as a new scaffold for synthesizing HOFs, as it inherently features multiple hydrogen-bonding motifs. This capability is clearly demonstrated in compounds **1–6**, and, more specifically, **3–6** meet the criteria for description as hydrogen-bonded frameworks. While hydrogen bonding in 2,5-PDC coordination polymers primarily relies on carboxylate groups interacting with coordinated or lattice water molecules,[84,85] 2,5-H_3PODC ligands in **1–6** feature H-bonding interactions involving all of the major functional groups: carboxylate, carbonyl, N–H groups, and coordinated water molecules. As both the hydrogen bond donors and acceptors are incorporated within a single ligand molecule, rather than distributed across multiple co-ligands or solvent molecules, 2,5-H_3PODC offers a valuable platform to promote structure-directing hydrogen bonding interactions without adding complexity to the reaction mixture. These ligand-centered hydrogen bonding interactions are more structurally integral than those involving solvent molecules, which are often lost during the activation of the networks, giving 2,5-H_3PODC a clear advantage as a structure-directing scaffold. Furthermore, the use of the 2,5-H_3PODC ligand has resulted in topologies that are rarely reported in the lanthanide materials literature,[79,88] highlighting another key advantage beyond its distinct coordination behavior and ligand-centered hydrogen bonding capabilities.

Thermogravimetric analysis (TGA)

The thermal stability of all compounds (**1–6**) was investigated using thermogravimetric analysis. Approximately 4–8 mg of each compound was placed in an alumina pan and heated from room temperature to 1000 °C at a rate of 10 °C min^{-1} in an air atmosphere (flow rate, 50 mL min^{-1}), with a second alumina pan used as the reference material. Thermal properties were consistent for each structure type so the TGA profiles of $[Pr(HPODC)(Ox)_{0.5}(H_2O)_2]$ (**1**) and $[Gd(H_2PODC)(HPODC)(H_2O)]$ (**4**) were used as representative examples and are described in detail. TGA curves for compounds **1–6** are shown in Fig. S28–S34 (SI). For compound **1**, the first weight loss of 9.02 wt% occurs from 110 °C to 275 °C (calcd 8.9%) is attributed to the loss of two coordinated water molecules. Subsequently, with increasing temperature, a more substantial weight loss of 49.33% occurs from 275 °C to 590 °C, which is a result of thermal decomposition of the organic ligand components of the coordination polymer network (calcd 50.02%). The thermal decomposition pattern of compound **4** differs with coordinated water loss not appearing as a distinct step and decomposition occurring progressively over a broad temperature interval from 134 °C to 738 °C, with a total weight loss of 65.29% (calcd 66.33%). After total weight losses of 58.35% for compound **1** and 65.29% for compound **4**, stoichiometric amounts of Pr_2O_3 and Gd_2O_3 are formed as the final residues, which were identified *via* powder X-ray diffraction.

Photoluminescence spectroscopy

Among the lanthanides, Eu(III) compounds are well known for their strong and characteristic luminescence, emitting red light in the 575–725 nm range.[89] Therefore, the solid-state luminescence properties of compound **3** were investigated at room temperature to ascertain whether 2,5-H_3PODC could act as an efficient antenna chromophore. Upon excitation at 368 nm (Fig. S41, SI), the emission spectrum of **3** displays several characteristic narrow emission bands in the 575–725 nm range, corresponding to the metal-centered 4f–4f transitions from the $^5D_0$ excited state of Eu(III) to the ^7F_J (J = 0–4) ground states, as shown in Fig. 7. More specifically, the five main spectral bands were observed at 579 nm, 588 nm, 619 nm, 650 nm, and 698 nm, which can be assigned to the $^5D_0 \rightarrow {}^7F_J$ (J = 0, 1, 2, 3, and 4) transitions of Eu(III), respectively. All the f–f transitions in the spectrum are formally Laporte forbidden induced electric dipole transitions, except for the $^5D_0 \rightarrow {}^7F_1$ transition, which is allowed by the magnetic dipole mechanism. Compound **3** exhibits intense red emission consistent with the high intensity sharp narrow band associ-

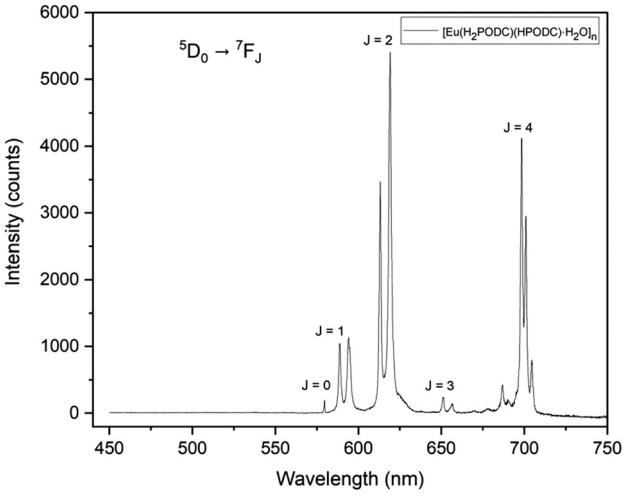

Fig. 7 Room temperature solid-state emission spectrum of compound **3** upon excitation at 368 nm.

ated with the $^5D_0 \rightarrow {}^7F_2$ transition. This spectral feature is especially sensitive to the local environment around the Eu(III) ion and the surrounding ligand field, and the high intensity of this peak for **3** indicates that the Eu(III) ions in this compound are in highly polarizable chemical environments lacking inversion symmetry.[89] Moreover, the emission intensity of the $^5D_0 \rightarrow {}^7F_2$ transition is approximately about 4.5 times that of the $^5D_0 \rightarrow {}^7F_1$ transition, which further indicates there is limited symmetry in the ligand field around the Eu(III) ion. Worthy of additional comment, the occurrence of intense, narrow, sharp spectral bands corresponding to the $^5D_0 \rightarrow {}^7F_4$ transition here is notable as it is typically seen as a low-intensity band in the photoluminescence spectra of the majority of the Eu-based coordination polymers reported in the literature.[90–96] According to several theoretical and experimental studies, this behavior is due to the highly polarizable local chemical environment and the slightly distorted D_{4d} geometry of the Eu (III) metal centers in **3**.[97–99] We also noted splitting of peaks corresponding to multiple f–f transitions, wherein two peaks were observed for the $^5D_0 \rightarrow {}^7F_1$, $^5D_0 \rightarrow {}^7F_2$, and $^5D_0 \rightarrow {}^7F_3$ bands, while the peak corresponding to the $^5D_0 \rightarrow {}^7F_4$ transition was split into three components. These peak splitting features are referred to as Stark components, which occur due to ligand field effects. When an Eu^{3+} ion is introduced into a chemical or ligand field environment, the degenerate J energy levels, originally $2J + 1$, undergo splitting into distinct Stark sub-levels due to the influence of the surrounding ligand and crystal fields. Therefore, the observed pattern confirms that the Eu(III) center in compound **3** is located in a non-spherically symmetric coordination environment, and strong binding interactions occur between the PODC ligands and the Eu(III) ions in **3**.

To better understand the photoluminescence properties of **3**, the relative fluorescence quantum yield (Φ) was calculated using $Na_3Eu(dipic)_3$ as a standard reference sample,[100–102] and details on the process for preparing the standard sample are included in the SI. The relative quantum yield for **3** was calculated by using eqn (S1) (SI) and the overall Φ value of 2.45% for **3** was significantly lower than the quantum yield of the $Na_3Eu(dipic)_3$ standard. The loss in emission efficiency for **3** is a likely result of the multiple –OH and –NH oscillators that are in close proximity to the Eu^{3+} metal center in **3** that allow for vibronic relaxation through –OH and –NH stretching modes.[103] Nevertheless, as a luminescent antenna, 2,5-H_3PODC shows promise as a chromophore with a relatively low energy excitation wavelength, comparable to those of the 2,5-PDC ligand-based lanthanide compounds, which is advantageous for many practical applications.[104–106]

Conclusions

This study presents the first successful incorporation of 2,5-H_3PODC as an organic linker in metal-containing coordination polymers. The synthetic pathway presented here offers a straightforward two-step route to obtain the ligand with high purity and a 79% overall yield. Six novel lanthanide coordination polymers were synthesized under solvothermal conditions, forming two distinct structure types, and both exhibited 2D network architectures with rectangular-shaped voids and dimensions of approximately 6 × 7 Å (**type 1**) and 6 × 9 Å (**type 2**). In **type 1** compounds, metal centers are bridged by oxalate ions in addition to PODC ligand moieties, and oxalic acid is generated *in situ via* a ring-opening/hydrolysis-oxidation mechanism. The structural divergence among **type 1** and **2** compounds arises from the lanthanide contraction, variations in ligand protonation states, and the *in situ* formation of oxalic acid. 2,5-H_3PODC ligands were found to exist in two different protonation states in **type 2** compounds, each exhibiting distinct coordination modes, and compared to conventional pyridine dicarboxylate ligands, 2,5-H_3PODC offers enhanced coordination, engaging in metal-binding not only through the carboxylate groups but also *via* pyridinone moieties. In the second coordination sphere, hydrogen bonding interactions involving carboxylate and pyridinone functional groups and coordinated water molecules further contribute to the structural stability of the synthesized compounds, and the dual functionality of 2,5-H_3PODC in metal coordination and hydrogen bonding underscores its ability to facilitate multiple routes for assembly of metal-ion SBUs including the formation of H-bonding frameworks in **3–6**. Thermogravimetric analysis (TGA) revealed that the compounds **1** and **4** exhibit structure-specific thermal behavior, reflecting distinct decomposition pathways that are unique to each structure type. Luminescence studies on compound **3** confirmed the ability of 2,5-H_3PODC to act as a luminescent antenna, thereby enabling observation of the characteristic f–f transitions of Eu(III) in the visible region. Overall, this work highlights the potential of pyridinone-based linkers for the further development of rare earth and f-element CPs and HOFs, and follow up studies with other PODC derivatives are underway.

Conflicts of interest

The authors declare no competing interests.

Data availability

All data for the article are included in the manuscript and supplementary information (SI). Supplementary information: detailed characterization of 2,5-H_3PODC: ^{1}H NMR, ^{13}C NMR, HRMS-ESI, PXRD, and infrared (MIR and FIR) spectra. For compounds **1–6**, crystallographic data, topological analysis details, PXRD patterns, FE-SEM/EDS data, TGA results, and MIR/FIR analyses are provided, and for **3**, the photoluminescence excitation spectrum and details related to quantum yield experiments are included. Insights into *in situ* oxalate formation including a proposed mechanism and HRMS-ESI analysis of solution mixtures, and synthesis procedures for pure-phase versions of compounds **1** and **2**, includ-

ing corresponding PXRD results, are provided as well. See DOI: https://doi.org/10.1039/d5dt02620b.

CCDC 2428551–2428556 (**1–6**) contain the supplementary crystallographic data for this paper.[107a–f]

Acknowledgements

This work was primarily supported by the University of Iowa, Office of the Provost, High Impact Hiring Initiative. AKKA, BL, and KPC also acknowledge support from start-up funds from the College of Liberal Arts and Sciences and the Department of Chemistry at the University of Iowa. AKKA would also like to thank University of Iowa Graduate College for a 2023 Summer Research Fellowship. BL acknowledges funding for this work provided by the U.S. Department of Energy, Office of Science, Office of Workforce Development for Teachers and Scientists, Office of Science Graduate Student Research (SCGSR) program. The SCGSR program is administered by the Oak Ridge Institute of Science and Education (ORISE). ORISE is managed by ORAU under contract number DE-SC0014664. Los Alamos National Laboratory is operated by Triad National Security, LLC, for the National Nuclear Security Administration of the U.S. Department of Energy (contract no. 89233218CNA000001). We also acknowledge the University of Iowa Materials, Analysis, Testing, and Fabrication (MATFab) Facility for use of the single crystal X-ray diffractometer, powder X-ray diffractometer, thermogravimetric analyzer, elemental analyzer, and scanning electron microscope used in this study. We would specifically like to thank MATFab staff member Dr. Michael Sinnwell for support associated with TGA, EA, and FE-SEM/EDS measurements. Single crystal XRD data were collected on an instrument funded by NSF Award CHE-1828117. Field emission SEM/EDS data were collected on an instrument funded by NSF Award EAR-2215495. The NMR instrument used in this research was supported by funding from the University of Iowa, while the mass spectrometry instrument was supported by funding from the NSF (CHE-1919422). Mid- and far-IR spectra were collected on an instrument funded by a Nuclear Regulatory Commission Faculty Development Grant (NRC 31310018M0042).

References

1 H. Zhang, G.-Y. Liu, X.-H. Diao, Y. Muhammad, C. Chen, Y.-Y. Gao, H. Wang, C.-S. Qi and W. Li, *J. Solid State Chem.*, 2023, **324**, 124114.
2 C. Lian, Y. Chen, S. Li, M.-Y. Hao, F. Gao and L.-R. Yang, *J. Alloys Compd.*, 2017, **702**, 303–308.
3 J. Rocha, L. D. Carlos, F. A. A. Paz and D. Ananias, *Chem. Soc. Rev.*, 2011, **40**, 926–940.
4 Z.-D. Zhou, C.-Y. Wang, G.-S. Zhu, B. Du, B.-Y. Yu and C.-C. Wang, *J. Mol. Struct.*, 2022, **1251**, 132009.
5 B. Chen, L. Wang, Y. Xiao, F. R. Fronczek, M. Xue, Y. Cui and G. Qian, *Angew. Chem.*, 2009, **121**, 508–511.
6 F.-Y. Yi, M. Gu, S.-C. Wang, J.-Q. Zheng, L. Pan and L. Han, *Inorg. Chem.*, 2018, **57**, 2654–2662.
7 L. Pan, K. M. Adams, H. E. Hernandez, X. Wang, C. Zheng, Y. Hattori and K. Kaneko, *J. Am. Chem. Soc.*, 2003, **125**, 3062–3067.
8 J. Duan, M. Higuchi, M. L. Foo, S. Horike, K. P. Rao and S. Kitagawa, *Inorg. Chem.*, 2013, **52**, 8244–8249.
9 H. Li, W. Shi, K. Zhao, Z. Niu, H. Li and P. Cheng, *Chem. – Eur. J.*, 2013, **19**, 3358–3365.
10 B. Li, H.-M. Wen, Y. Cui, G. Qian and B. Chen, *Prog. Polym. Sci.*, 2015, **48**, 40–84.
11 C. Pagis, M. Ferbinteanu, G. Rothenberg and S. Tanase, *ACS Catal.*, 2016, **6**, 6063–6072.
12 Y. Zhang, S. Liu, Z.-S. Zhao, Z. Wang, R. Zhang, L. Liu and Z.-B. Han, *Inorg. Chem. Front.*, 2021, **8**, 590–619.
13 C. Xu, Y. Liu, L. Wang, J. Ma, L. Yang, F.-X. Pan, A. M. Kirillov and W. Liu, *Dalton Trans.*, 2017, **46**, 16426–16431.
14 M. Sinchow, N. Semakul, T. Konno and A. Rujiwatra, *ACS Sustainable Chem. Eng.*, 2021, **9**, 8581–8591.
15 W.-M. Wang, R.-R. Cheng, Z.-L. Wu and J.-Z. Cui, *Inorg. Chem.*, 2023, **62**, 14902–14911.
16 J.-C. G. Bünzli, *J. Coord. Chem.*, 2014, **67**, 3706–3733.
17 K. P. Carter and C. L. Cahill, in *Handbook on the Physics and Chemistry of Rare Earths*, ed. J.-C. G. Bünzli and V. K. Pecharsky, Elsevier, Amsterdam, 2015, vol. 47, pp. 147–208.
18 T. Qin, Z. Shi, W. Zhang, X. Dong, N. An, H. Sakiyama, M. Muddassir, D. Srivastava and A. Kumar, *J. Mol. Struct.*, 2023, **1282**, 135220.
19 Y.-G. Huang, F.-L. Jiang and M.-C. Hong, *Coord. Chem. Rev.*, 2009, **253**, 2814–2834.
20 J.-Q. Liu, Z.-D. Luo, Y. Pan, A. K. Singh, M. Trivedi and A. Kumar, *Coord. Chem. Rev.*, 2020, **406**, 213145.
21 A. Wang, Y. Zhang, L. Lu, M. Zhu, C. Yuan and S. Feng, *Dalton Trans.*, 2022, **51**, 12324–12333.
22 Y. Hasegawa and Y. Kitagawa, *J. Photochem. Photobiol., C*, 2022, **51**, 100485.
23 M. Yawer, M. Kariem, P. Sood and H. N. Sheikh, *CrystEngComm*, 2016, **18**, 3617–3634.
24 S. L. Cai, S. R. Zheng, J. Fan, J. B. Tan, T. T. Xiao and W.-G. Zhang, *J. Solid State Chem.*, 2011, **184**, 3172–3178.
25 S.-J. Wang, Y. Liu, Z.-Q. Zhang, Q. Li, G. Xiong, L.-X. You and Y. Sun, *Aust. J. Chem.*, 2023, **77**, CH23149.
26 M. Kumar, H. N. Sheikh, A. Fraconetti, J. K. Zaręba, S. C. Sahoo and A. Frontera, *New J. Chem.*, 2019, **43**, 2179–2195.
27 S.-R. Zheng, S.-L. Cai, M. Pan, J. Fan, T.-T. Xiao and W.-G. Zhang, *CrystEngComm*, 2011, **13**, 883–888.
28 N. A. Ashashi, C. Sen, M. Ahmad, A. K. Jassal and H. N. Sheikh, *J. Solid State Chem.*, 2024, **334**, 124659.
29 D. Vlasyuk, R. Łyszczek, L. Mazur, A. Pladzyk, Z. Hnatejko and P. Woźny, *Molecules*, 2023, **28**, 6360.
30 B. Zhao, X.-Y. Chen, P. Cheng, D.-Z. Liao, S.-P. Yan and Z.-H. Jiang, *J. Am. Chem. Soc.*, 2004, **126**, 15394–15395.

31 L.-X. You, B.-Y. Ren, Y.-K. He, S.-J. Wang, Y.-G. Sun, V. Dragutan, G. Xiong and F. Ding, *J. Mol. Struct.*, 2024, 137687.
32 C. Daiguebonne, N. Kerbellec, O. Guillou, J.-C. Bünzli, F. Gumy, L. Catala, T. Mallah, N. Audebrand, Y. Gérault and K. Bernot, *Inorg. Chem.*, 2008, **47**, 3700–3708.
33 N. Kerbellec, D. Kustaryono, V. Haquin, M. Etienne, C. Daiguebonne and O. Guillou, *Inorg. Chem.*, 2009, **48**, 2837–2843.
34 C. Daiguebonne, N. Kerbellec, Y. Gérault and O. Guillou, *J. Alloys Compd.*, 2008, **451**, 372–376.
35 Y.-F. Zhou, F.-L. Jiang, Y. Xu, R. Cao and M.-C. Hong, *J. Mol. Struct.*, 2004, **691**, 191–195.
36 P. R. Donnarumma, S. Frojmovic, P. Marino, H. A. Bicalho, H. M. Titi and A. J. Howarth, *Chem. Commun.*, 2021, **57**, 6121–6124.
37 P. R. Donnarumma, C. Copeman, M. Richezzi, J. Sardilli, H. M. Titi and A. J. Howarth, *Cryst. Growth Des.*, 2024, **24**, 1619–1625.
38 T. Gorai, W. Schmitt and T. Gunnlaugsson, *Dalton Trans.*, 2021, **50**, 770–784.
39 Y. Wang, S.-H. Xing, F.-Y. Bai, Y.-H. Xing and L.-X. Sun, *Inorg. Chem.*, 2018, **57**, 12850–12859.
40 Y.-M. Zhu, C.-H. Zeng, T.-S. Chu, H.-M. Wang, Y.-Y. Yang, Y.-X. Tong, C.-Y. Su and W.-T. Wong, *J. Mater. Chem. A*, 2013, **1**, 11312–11319.
41 N. E. Greig, J. D. Einkauf, J. M. Clark, E. J. Corcoran, J. P. Karram, C. A. Kent, V. E. Eugene, B. C. Chan and D. T. De Lill, *J. Solid State Chem.*, 2015, **225**, 402–409.
42 Z. ul Nisa, L. Tashi, C. Sen, N. A. Ashashi, S. C. Sahoo and H. N. Sheikh, *New J. Chem.*, 2020, **44**, 8125–8137.
43 M. Kumar, L.-Q. Li, J. K. Zaręba, L. Tashi, S. C. Sahoo, M. Nyk, S.-J. Liu and H. N. Sheikh, *Cryst. Growth Des.*, 2020, **20**, 6430–6452.
44 Z.-Q. Shi, N.-N. Ji, L.-L. Lan, T. Zhang, H.-L. Hu and G. Li, *Coord. Chem. Rev.*, 2023, **493**, 215300.
45 M. Sato, T. Ishigaki, M. Iwaki, K. Uematsu, M. Watanabe and K. Toda, *Inorg. Chem.*, 2021, **60**, 17810–17823.
46 R.-F. Li, R.-H. Li, X.-F. Liu, X.-H. Chang and X. Feng, *RSC Adv.*, 2020, **10**, 6192–6199.
47 M. Kumar, M. Kariem, H. N. Sheikh, A. Frontera, S. K. Seth and A. K. Jassal, *Dalton Trans.*, 2018, **47**, 12318–12336.
48 A. Khurshid, T. Chuasaard, M. Sinchow, A. Ngamjarurojana and A. Rujiwatra, *J. Solid State Chem.*, 2025, **341**, 125082.
49 W. Lu, Z. Wei, Z.-Y. Gu, T.-F. Liu, J. Park, J. Park, J. Tian, M. Zhang, Q. Zhang, T. Gentle III, M. Bosch and H.-C. Zhou, *Chem. Soc. Rev.*, 2014, **43**, 5561–5593.
50 S. Yuan, Y.-P. Chen, J.-S. Qin, W. Lu, L. Zou, Q. Zhang, X. Wang, X. Sun and H.-C. Zhou, *J. Am. Chem. Soc.*, 2016, **138**, 8912–8919.
51 S. Wu, D. Ren, K. Zhou, H.-L. Xia, X.-Y. Liu, X. Wang and J. Li, *J. Am. Chem. Soc.*, 2021, **143**, 10547–10552.
52 V. V. Torbina, Y. A. Belik and O. V. Vodyankina, *React. Chem. Eng.*, 2025, **10**, 1197–1215.
53 J. Zhao, Y.-N. Wang, W.-W. Dong, Y.-P. Wu, D.-S. Li and Q.-C. Zhang, *Inorg. Chem.*, 2016, **55**, 3265–3271.
54 L.-H. Liu, X.-T. Qiu, Y.-J. Wang, Q. Shi, Y.-Q. Sun and Y.-P. Chen, *Dalton Trans.*, 2017, **46**, 12106–12113.
55 J.-N. Hao and B. Yan, *J. Mater. Chem. C*, 2014, **2**, 6758–6764.
56 Y. Zhang, Y. Wang, L. Liu, N. Wei, M.-L. Gao, D. Zhao and Z.-B. Han, *Inorg. Chem.*, 2018, **57**, 2193–2198.
57 X. Zhang, J. Yu, X. Li, C. Jiao, Y. Zhu, H. Zheng and Z. Sun, *J. Mater. Chem. C*, 2024, **12**, 18829–18839.
58 S. Ganguly, P. Pachfule, S. Bala, A. Goswami, S. Bhattacharya and R. Mondal, *Inorg. Chem.*, 2013, **52**, 3588–3590.
59 Y. G. Sun, S. T. Rong, W. Yu, Y. L. Wu, F. Ding, E. J. Gao, W. Z. Zhang and F. Verpoort, *Z. Anorg. Allg. Chem.*, 2009, **635**, 2585–2591.
60 H.-L. Gao, L. Yi, B. Zhao, X.-Q. Zhao, P. Cheng, D.-Z. Liao and S.-P. Yan, *Inorg. Chem.*, 2006, **45**, 5980–5988.
61 T. Devic, P. Horcajada, C. Serre, F. Salles, G. Maurin, B. Moulin, D. Heurtaux, G. Clet, A. Vimont and J.-M. Greneche, *J. Am. Chem. Soc.*, 2010, **132**, 1127–1136.
62 F. Ngom, A. Chang, C. Blais, C. Daiguebonne, Y. Suffren, M. Camara, G. Calvez, K. Bernot and O. Guillou, *Inorg. Chem.*, 2024, **63**, 13048–13058.
63 L. Razquin-Bobillo, A. Zabala-Lekuona, J. A. García, A. Rodríguez-Diéguez and J. Cepeda, *Adv. Opt. Mater.*, 2024, 2401472.
64 L. Razquin-Bobillo, O. Pajuelo-Corral, A. Zabala-Lekuona, A. Rodríguez-Diéguez and J. Cepeda, *Dalton Trans.*, 2022, **51**, 16243–16255.
65 J. M. Domagala, *J. Org. Chem.*, 1984, **49**, 126–130.
66 J. R. Blanton, R. J. Papoular and D. Louër, *Powder Diffr.*, 2019, **34**, 233–241.
67 *OriginPro, Version 2024b*, Origin Lab Corporation, Northampton, MA, USA.
68 D. Tatum, J. Xu, D. Magda and N. Butlin, *US Pat*, 10239878B2, 2019.
69 *APEX5*, Bruker AXS Inc., Madison, WI, USA, 2024.
70 G. M. Sheldrick, *Acta Crystallogr., Sect. A:Found. Adv.*, 2015, **71**, 3–8.
71 G. M. Sheldrick, *Acta Crystallogr., Sect. C:Struct. Chem.*, 2015, **71**, 3–8.
72 O. V. Dolomanov, L. J. Bourhis, R. J. Gildea, J. A. Howard and H. Puschmann, *J. Appl. Crystallogr.*, 2009, **42**, 339–341.
73 D. Palmer, *CrystalMaker®*, CrystalMaker Software Ltd., Begbroke, Oxfordshire, England, 2024.
74 C. F. Macrae, I. Sovago, S. J. Cottrell, P. T. Galek, P. McCabe, E. Pidcock, M. Platings, G. P. Shields, J. S. Stevens and M. Towler, *Appl. Crystallogr.*, 2020, **53**, 226–235.
75 V. A. Blatov, A. P. Shevchenko and D. M. Proserpio, *Cryst. Growth Des.*, 2014, **14**, 3576–3586.
76 R.-H. Hu, S.-Z. Liu, Y.-Y. Xu, X.-G. Yi, W.-T. Chen and W.-S. Lin, *J. Mol. Struct.*, 2022, **1265**, 133396.

77 K. E. Knope, H. Kimura, Y. Yasaka, M. Nakahara, M. B. Andrews and C. L. Cahill, *Inorg. Chem.*, 2012, **51**, 3883–3890.
78 C. R. Groom, I. J. Bruno, M. P. Lightfoot and S. C. Ward, *Acta Crystallogr., Sect. B:Struct. Sci., Cryst. Eng. Mater.*, 2016, **72**, 171–179.
79 A. P. Shevchenko, A. A. Shabalin, I. Y. Karpukhin and V. A. Blatov, *Sci. Technol. Adv. Mater.: Methods*, 2022, **2**, 250–265.
80 X. Li, X.-S. Wu and X.-J. Zheng, *Inorg. Chim. Acta*, 2009, **362**, 2537–2541.
81 P. Silva, L. Cunha-Silva, N. J. Silva, J. Rocha and F. A. A. Paz, *Cryst. Growth Des.*, 2013, **13**, 2607–2617.
82 P. C. Soares-Santos, L. Cunha-Silva, F. A. A. Paz, R. A. S. Ferreira, J. Rocha, T. Trindade, L. D. Carlos and H. I. Nogueira, *Cryst. Growth Des.*, 2008, **8**, 2505–2516.
83 B. Ay, E. Yildiz, M. Enomoto, A. Okazawa and N. Kojima, *Polyhedron*, 2022, **226**, 116110.
84 M. S. Abdelbaky, Z. Amghouz, E. Fernández-Zapico, S. García-Granda and J. R. García, *J. Solid State Chem.*, 2015, **229**, 197–207.
85 M. Sinchow, T. Chuasaard, B. Yotnoi and A. Rujiwatra, *J. Solid State Chem.*, 2019, **278**, 120902.
86 Z. Zhang, Y. Ye, S. Xiang and B. Chen, *Acc. Chem. Res.*, 2022, **55**, 3752–3766.
87 P. Li, M. R. Ryder and J. F. Stoddart, *Acc. Mater. Res.*, 2020, **1**, 77–87.
88 F. H. Allen and K. J. Lipscomb, in *Encyclopedia of Supramolecular Chemistry*, ed. J. L. Atwood and J. W. Steed, CRC Press, Boca Raton, 2013, vol. 1, pp. 161–168.
89 K. Binnemans, *Coord. Chem. Rev.*, 2015, **295**, 1–45.
90 X. Song, Y. Ma, X. Ge, H. Zhou, G. Wang, H. Zhang, X. Tang and Y. Zhang, *RSC Adv.*, 2017, **7**, 8661–8669.
91 D. Wang, C. Zheng, L. Fan, J. Zheng and X. Wei, *Synth. Met.*, 2012, **162**, 2063–2068.
92 L. Dewez, S. Hommada, Y. Suffren and N. Audebrand, *Inorg. Chim. Acta*, 2025, **579**, 122583.
93 M. Sengar and A. K. Narula, *Sens. Actuators, B*, 2017, **241**, 567–576.
94 L. Zhang, D. Xu, Y. Zhou and F. Jiang, *New J. Chem.*, 2010, **34**, 2470–2478.
95 C.-G. Wang, Y.-H. Xing, Z.-P. Li, J. Li, X.-Q. Zeng, M.-F. Ge and S.-Y. Niu, *Cryst. Growth Des.*, 2009, **9**, 1525–1530.
96 Q. Shi, S. Zhang, Q. Wang, H. Ma, G. Yang and W.-H. Sun, *J. Mol. Struct.*, 2007, **837**, 185–189.
97 G. Souadi, Ü. H. Kaynar, M. Ayvacikli and N. Can, *Appl. Radiat. Isot.*, 2023, **199**, 110905.
98 F. Sa, S. Nobre, C. Granadeiro, H. Nogueira, L. Carlos and O. Malta, *J. Lumin.*, 2006, **121**, 561–567.
99 L. L. Devi and C. Jayasankar, *Ceram. Int.*, 2018, **44**, 14063–14069.
100 A. M. Brouwer, *Pure Appl. Chem.*, 2011, **83**, 2213–2228.
101 C. Würth, D. Geißler, T. Behnke, M. Kaiser and U. Resch-Genger, *Anal. Bioanal. Chem.*, 2015, **407**, 59–78.
102 J. Hu and C.-Y. Zhang, *Anal. Chem.*, 2013, **85**, 2000–2004.
103 M. J. J. Mangnus, V. R. M. Benning, B. Baumgartner, P. T. Prins, T. P. van Swieten, A. J. H. Dekker, A. van Blaaderen, B. M. Weckhuysen, A. Meijerink and F. T. Rabouw, *Nanoscale*, 2023, **15**, 16601–16611.
104 A. K. Singh, *Coord. Chem. Rev.*, 2022, **455**, 214365.
105 G. Tessitore, G. A. Mandl, S. L. Maurizio, M. Kaur and J. A. Capobianco, *RSC Adv.*, 2023, **13**, 17787–17811.
106 C. Alexander, Z. Guo, P. B. Glover, S. Faulkner and Z. Pikramenou, *Chem. Rev.*, 2025, **125**, 2269–2370.
107 (*a*) CCDC 2428551: Experimental Crystal Structure Determination, 2025, DOI: 10.5517/ccdc.csd.cc2mj3cn.; (*b*) CCDC 2428552: Experimental Crystal Structure Determination, 2025, DOI: 10.5517/ccdc.csd.cc2mj3dp; (*c*) CCDC 2428553: Experimental Crystal Structure Determination, 2025, DOI: 10.5517/ccdc.csd.cc2mj3fq; (*d*) CCDC 2428554: Experimental Crystal Structure Determination, 2025, DOI: 10.5517/ccdc.csd.cc2mj3gr; (*e*) CCDC 2428555: Experimental Crystal Structure Determination, 2025, DOI: 10.5517/ccdc.csd.cc2mj3hs; (*f*) CCDC 2428556: Experimental Crystal Structure Determination, 2025, DOI: 10.5517/ccdc.csd.cc2mj3jt.